ELECTROCHEMICAL CHARACTERIZATION OF PURE AND NITROGEN-CONTAINING ANODIC TiO_2 NANOCOLUMN ARRAYS

LEDNICKÝ Tomáš, MOZALEV Alexander, BENDOVA Maria*

Brno University of Technology, CEITEC - Central European Institute of Technology, Brno, Czech Republic, EU
* maria.bendova@ceitec.vutbr.cz

Abstract

TiO_2 nanocolumn arrays are prepared via porous-anodic-alumina-assisted anodizing of Al/Ti or Al/TiN_x layers in an oxalic acid electrolyte. The upper Al layer is anodized at 40 V to form a nanoporous anodic film; then the Ti or TiN_x underlayer is re-anodized to 100 V. This leads to the growth of anodic TiO_2 or N-containing TiO_2 nanocolumns within the alumina pores, which are approx. 40 nm wide and 160 nm long. The crystallinity and doping degree of the nanocolumns are modified by the annealing in air or vacuum at 600°C. Cyclic voltammetry, electrochemical impedance spectroscopy, and Mott-Schottky analysis revealed n-type semiconducting properties of the N-doped nanocolumns whereas most of the undoped TiO_2 nanocolumns exhibited dielectric behavior. The calculated doping concentration and the flat-band potential vary with the annealing conditions. This allows for controlled alteration of the depletion layer thickness in order to enhance the photoelectrochemical water-splitting ability of the films by improving photogenerated charge carrier separation and band-gap tuning. The N-containing nanocolumns appeared to possess trap states, as manifested by Fermi level pining, which may provide additional benefits for heterogeneous charge-carrier transport for water oxidation.

Keywords: Porous anodic alumina, anodizing, Mott-Schottky analysis, photoelectrochemical water splitting

1. INTRODUCTION

Nanostructured titanium dioxide has been studied extensively as photoanode material for water oxidation thanks to its high chemical and thermal stability, low costs, high abundance, as well as band edges being favorably aligned with water redox potentials [1-4]. However, the relatively large bandgap (3.0 eV for rutile and 3.2 eV for anatase [5]) and the low electron conductivity (0.3 $cm^2 \cdot V^{-1} \cdot s^{-1}$ [6]) have limited its widespread utilization [7, 8]. In recent years, extensive efforts have been applied to employ TiO_2 as photoelectrode material in photoelectrochemical (PEC) cells for solar-driven water splitting. To improve its efficiency, several fundamental directions are being explored: (i) increasing the absorption of solar energy through reduction of the band gap by band-gap engineering, (ii) reducing the energy losses caused by poor charge transport through enhancing the charge carrier conductivity, and (iii) reducing the energy losses associated with charge recombination by introducing internal electric fields (e.g. a depletion layer at the semiconductor surface) required for effective charge separation [9, 5].

In this work, we have prepared arrays of N-free and N-doped TiO_2 nanocolumns by porous-anodic-alumina (PAA)-assisted anodizing of Ti [10, 11] or TiN_x [12] thin films embedded in the PAA and studied their electrochemical properties by means of cyclic voltammetry, electrochemical impedance spectroscopy (EIS), and Mott-Schottky (M-S) analysis with respect to the nitrogen concentration and annealing conditions, in order to reveal the influence of formation conditions on the conductivity, doping level, and depletion (space charge) layer thickness. The results will provide a better understanding of how N-doping or annealing affects semiconducting properties of the nanocolumn arrays prepared by PAA-assisted anodizing.

2. EXPERIMENTAL PART

The nanocolumn arrays were prepared via anodizing of Al/Ti or Al/TiN$_x$ bilayers (approx. 20 at.% of nitrogen mixed with titanium) sputter-deposited on oxidized silicon wafers [10-12] (hereafter N-free and N-doped, respectively). The anodizing and re-anodizing were performed in a through-flow two-electrode electrochemical cell with a stainless steel counter electrode in 0.3 mol·dm^{-3} oxalic acid at 22 °C. The layer of Al was anodized potentiostatically at 40 V, this being followed by a potentiodynamic re-anodizing of the underlying Ti or TiN$_x$ to 100 V. Afterwards, some of the samples were annealed in the ambient atmosphere or in vacuum (10^{-4} Pa) at 600 °C for two hours, which resulted in three types of nanocolumns (as-anodized, air-annealed, or vacuum-annealed) prepared from the two precursor underlayers.

Electrochemical characterization (cyclic voltammetry, EIS, and M-S analysis) was carried out in a borate buffer (0.5 mol·dm^{-3} H_3BO_3, 0.5 mol·dm^{-3} $Na_2B_4O_7$ aqueous solution, pH 7.4) at 22 °C in the dark. A μAutolab III/FRA2 Metrohm Autolab Potentiostat/Galvanostat was used as the potentiostat and impedance analyzer. A three-electrode setup was employed with a sample connected as working electrode, an Ag/AgCl reference electrode, and a gold sheet as counter electrode. For cyclic voltammetry, the current response was measured in a potential range from –0.56 to 1.44 V *vs.* RHE, with a scan rate of 50 mV·s^{-1} starting from open-circuit potential. The EIS measurements were performed from 1.44 to –0.56 V *vs.* RHE over a frequency range from 10 kHz to 0.1 Hz with 10 mV excitation amplitude. The impedance data were analyzed by computer simulation and fitting in Autolab Nova Software.

3. RESULTS AND DISCUSSION

Figure 1a-c shows schematically the preparation of TiO_2 nanocolumn arrays embedded in a PAA matrix via anodizing/re-anodizing of an Al/Ti (Al/TiN$_x$) bilayer [10-12], as described in Experimental Part. The nanocolumns grow inside the alumina nanopores, and their geometrical parameters can be tuned by varying the formation conditions. In this study, we prepare one possible type of their morphology shown in a scanning electron microscopy (SEM) image in **Figure 1d** at circumstances of varying their crystallinity and oxygen concentration by the annealing conditions, in order to alter their semiconducting properties, especially the doping level.

Cyclic voltammograms obtained at low voltages for the as-anodized, air-annealed, and vacuum-annealed nanocolumn arrays prepared from the N-free and N-doped titanium underlayers are shown in **Figure 2a, b**. Several trends are noticed: (1) for both the N-free and N-doped underlayers, the current density (thus also the conductivity) depends on the annealing conditions and increases in the order as-anodized < air-annealed < vacuum-annealed samples, (2) for all the conditions, the current density is higher for the N-doped samples as compared with the N-free surfaces, (3) the *I-V* curves are asymmetric for most of the samples, with lower anodic current densities as compared with the cathodic ones. Besides, when measured to more anodic voltages (**Figure 2c**), the vacuum-annealed N-free and N-doped samples show a substantially higher current

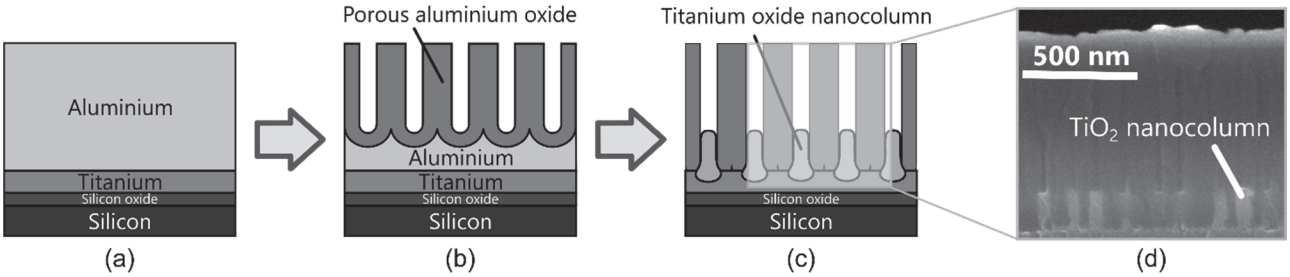

Figure 1 (a-c) Schematic illustration of PAA-assisted anodizing of an Al/Ti bilayer resulting in the formation of PAA-embedded TiO_2 nanocolumns. (d) A cross-sectional SEM image showing an example of PAA-embedded TiO_2 nanocolumns, approx. 40 nm wide and 160 nm long

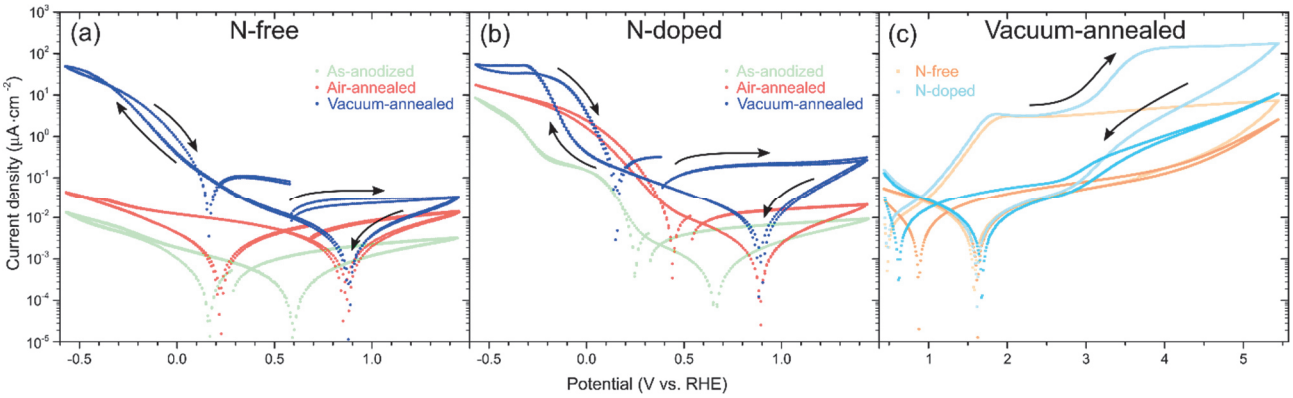

Figure 2 Cyclic voltammograms obtained at low voltages in the borate buffer in the dark for the (a) N-free and (b) N-doped TiO_2 nanocolumn arrays, both of them as-anodized, air-annealed, and vacuum-annealed. (c) Cyclic voltammograms of the vacuum-annealed N-free and N-doped arrays obtained at higher anodic potentials. The first measured cycle of each sample is shown by pale blue or pale orange color. The absolute value of current density is used. The arrows point out the measurement direction

density in the initial than in the consecutive measurement cycles, reaching two plateaus at 1.7 V *vs.* RHE of 3 μA·cm^{-2} for both samples and at 3.5 V *vs.* RHE of 150 μA·cm^{-2} only for the N-doped sample. These plateaus are not present in the consecutive measurement cycles, however, the N-doped surface still reveals a substantial current density rise at about 3.5 V *vs.* RHE, corresponding to the second plateau. The air-annealed and as-anodized arrays of the two N contents do not show these features and have the current densities of 1-2 orders of magnitude lower (about 0.1 μA·cm^{-2} at 5.5 V *vs.* RHE, not shown).

In addition, voltage-dependent EIS measurements were performed for all array types, in order to gain insight into their semiconducting properties. Two sets of measured EIS data for the two air-annealed samples are presented in **Figure 3** in the form of Bode plots. All EIS data were fit in the whole frequency range using an equivalent electrical circuit composed of one or two capacitive layers in series (shown as insets of **Figure 3**). One of the capacitances usually corresponds to the space-charge layer formed at the top of the columns, another one, with the higher capacitance and lower resistance, is attributed to the Helmholtz layer [13]. A constant phase element (CPE) is used to account for non-ideal behavior of the space-charge layer. M-S plots for all the samples are obtained by plotting C_{SCL}^{-2} *vs.* potential (see **Figure 4**), where the doping density

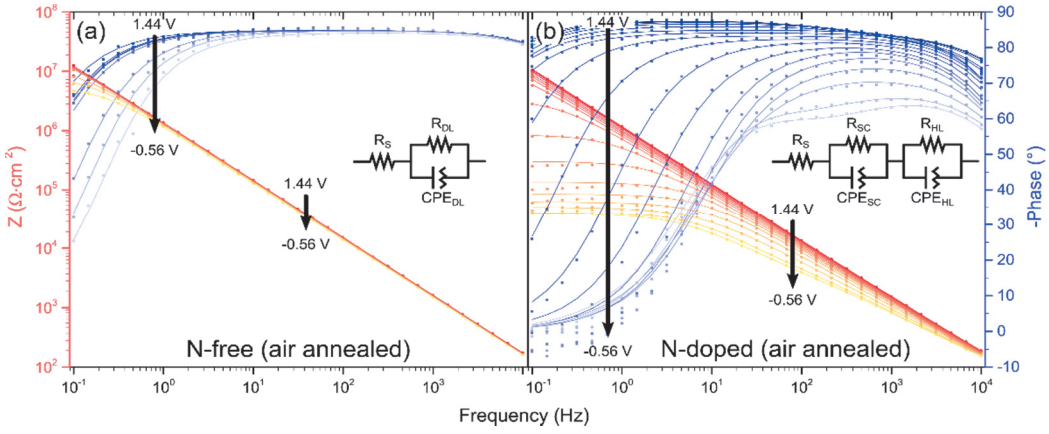

Figure 3 Bode plot representations of EIS measurements of the (a) N-free and (b) N-doped air-annealed nanoarrays obtained in the borate buffer at DC voltages from 1.44 to –0.56 V *vs.* RHE. The measured data are represented by dots, whereas the solid lines are the fits by equivalent electrical circuits shown as insets (SC = space charge layer, HL = Helmholtz layer, DL = dielectric layer)

N_d can be obtained from the slope of the linear part according to the M-S relation for n-type semiconductors:

$$\left(\frac{C_{SCL}}{A}\right)^{-2} = \left(\frac{2}{e\varepsilon_r\varepsilon N_d}\right)\left(E - E_{fb} - \frac{k_B T}{e}\right), \quad (1)$$

where C_{SCL}/A is the capacitance of the space charge layer per area, e is the elementary charge, ε is the vacuum permittivity, ε_r is the relative permittivity of TiO_2 ($\varepsilon_r = 70$), E is the applied potential, E_{fb} is the flatband potential, k_B is the Boltzman constant, and T is the temperature. Two types of behavior can be distinguished. First, a relatively constant capacitance, independent on the potential, is revealed for the N-free as-anodized and air-annealed samples (M-S plots in **Figure 4a, b**). This is seen also in the corresponding Bode plots (**Figure 3a**), where the impedance modulus and phase curves overlap for all potentials. This kind of behavior is typical for dielectrics. The second type is observed for all N-doped arrays and the vacuum-annealed N-free sample, with a positive slope and saturated marginal regions in the M-S plots (**Figure 4**), typical for n-type semiconductors. The corresponding Bode plot (**Figure 3b**) shows clearly that both the impedance modulus and phase shift change substantially with the potential. In addition, the slope in the M-S plots is divided into two parts by a plateau, which can be most easily distinguished for the N-doped air-annealed array (**Figure 4b**), giving a pair of N_d and V_{fb} values for each sample.

For those arrays that reveal n-type semiconducting behavior, we calculate N_d from Equation 1, *i.e.* from the slope of the corresponding M-S plot as marked in **Figure 4** (the slope at the more cathodic potential is used), taking into account the electrochemically active area (the column tops, not the PAA matrix), being about 11% of the apparent area, and assuming the same value of $\varepsilon_r = 70$ for both N contents. The results are shown in **Figure 5a**. Also, the depletion layer thickness (eventually the dielectric layer thickness) is calculated from the capacitance obtained from EIS at 1.44 V *vs.* RHE, taking 11% of the apparent area and $\varepsilon_r = 70$ for both N contents and neglecting the influence of the PAA (see **Figure 5b**). The M-S analysis therefore shows that most of the samples reveal clearly n-type semiconducting behavior, with N_d increasing in the order as-anodized < air-annealed < vacuum-annealed N-doped arrays (**Figure 5a**).

We expected the same trend for the N-free surfaces, but rather dielectric behavior is revealed for the as-anodized and air-annealed samples. There may be another explanation for the dielectric behavior of these two array types. Provided they are semiconducting and have a low value of N_d, the depletion layer may extend into the whole column length and the applied cathodic potential may not be cathodic enough to shrink the depletion layer to the column tops and to reach the flat-band conditions, as is the case of the other arrays, having higher N_d. The thickness of the depletion/dielectric layer as calculated from the measured capacitance supports this consideration. To eventually prove this, EIS measurements at more negative potentials are needed.

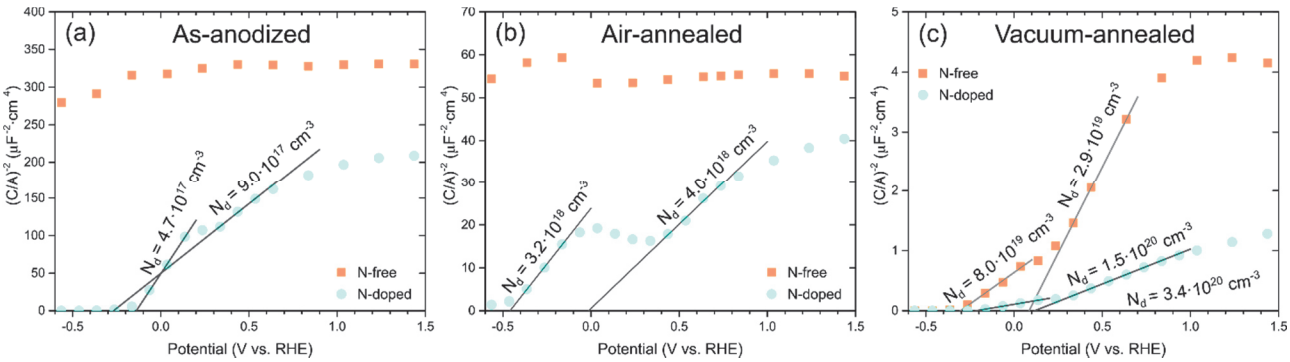

Figure 4 Mott-Schottky plots calculated from fits of the potential-dependent EIS measurements

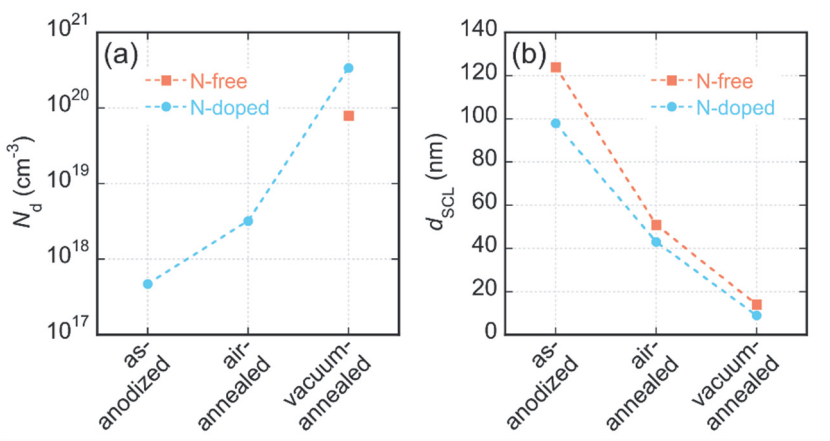

Figure 5 (a) Donor density N_d calculated for the different types of TiO_2 nanocolumn arrays from the Mott-Schottky plots. (b) Depletion layer thickness calculated from the capacitance obtained by EIS measurements at 1.44 V *vs.* RHE

Two main conclusions come out from the M-S analysis. Both the annealing treatment and the doping with nitrogen affect the donor density in the TiO_2 nanocolumns, influencing their electron conductivity, while N_d increases in the order as-anodized < air-annealed < vacuum-annealed samples and the N-free < N-doped arrays. This is in a good agreement with the cyclic voltammetry results, where the current density (also the conductivity) shows the same trends (**Figure 2a, b**). The altering of N_d-value via changing the annealing conditions is consistent with the literature reports demonstrating that a thermal treatment of TiO_2 in oxygen-deficient environments leads to creation of oxygen vacancies (V_O) in the material, which act as shallow donors and lead to n-type semiconducting behavior [7, 11]. This effect depends mainly on the annealing temperature, the initial V_O concentration in the sample, and the partial O_2 pressure in the gas phase [9]. Therefore, the loss of oxygen is more pronounced by the annealing in vacuum than in ambient atmosphere. In addition, the vacuum annealing seems to lead to a substantial reduction of the columns, as we observe their re-oxidation during cyclic voltammetry to higher anodic potentials (**Figure 2c**), as manifested by the lower current density plateau of about 3 $\mu A \cdot cm^{-2}$ present for the vacuum-annealed nanoarrays.

The presence of nitrogen in the TiO_2 nanocolumns increases the measured donor density and also the conductivity for all the annealing treatments. N doping is known to narrow the band gap of TiO_2 [5], which enhances the visible light absorption. Also, N doping may lead to formation of impurity states within the band gap of TiO_2 [5]. The M-S analysis of the N-doped arrays performed in this work shows a distinct plateau (best visible for the air-annealed sample shown in **Figure 4b**), which may be attributed to Fermi level pinning due to trap states [15]. This may be an indication of the prevailing N-doping mechanism. In addition, the second plateau, appearing during the cyclic voltammetry to higher anodic potentials (about 150 $\mu A \cdot cm^{-2}$) only for the N-doped vacuum-annealed sample, may reveal information about the chemical state of nitrogen in the anodic films. Detailed investigation of these effects is being carried out. Beside the effects described above, the crystallinity of the arrays may have substantial influence on the semiconducting properties and conductivity of the columns. This will be addressed in a future study.

4. CONCLUSIONS

Electrochemical properties of N-free and N-doped TiO_2 nanocolumns prepared via PAA-assisted anodizing and post-anodizing annealing in different atmospheres have been studied. Cyclic voltammetry and Mott-Schottky analysis have revealed that the incorporation of nitrogen and the annealing at oxygen-deficient conditions lead to a significant rise of n-type donor concentration in the titanium-oxide nanocolumns, which is thus tunable by several orders of magnitude. The space charge layer thickness can be adjusted accordingly.

The present findings are of vast importance for future utilization of the TiO_2-based nanocolumn arrays for photoelectrochemical water splitting, in order to obtain nanocolumns with good electrical conductivity and a space charge layer localized at the column surface, so as to substantially enhance the photogenerated charge carrier separation in these nanoarrays.

ACKNOWLEDGEMENTS

Research leading to these results was supported by GAČR grant no. 15-23005Y.

REFERENCES

[1] FUJISHIMA, A., ZHANG, X., TRYK, D. TiO_2 photocatalysis and related surface phenomena. *Surface Science Reports*, 2008, vol. 63, pp. 515-582.

[2] NAKATA, K., FUJISHIMA, A. TiO_2 photocatalysis: Design and applications. *Journal of Photochemistry and Photobiology C: Photochemistry Reviews*, 2012, vol. 13, pp. 169-189.

[3] GANDUGLIA-PIROVANO, M. V., HOFMANN, A., SAUER, J. Oxygen vacancies in transition metal and rare earth oxides: Current state of understanding and remaining challenges. *Surface Science Reports*, 2007, vol. 62, pp. 219-270.

[4] SCHNEIDER, J., MATSUOKA, M., TAKEUCHI, M., ZHANG, J., HORIUCHI, Y., ANPO, M., BAHNEMANN, D. W. Understanding TiO_2 Photocatalysis: Mechanisms and Materials. *Chemical Reviews*, 2014, vol. 114, pp. 9919-9986.

[5] ASAHI, R., MORIKAWA, T., IRIE, H., OHWAKI, T. Nitrogen-Doped Titanium Dioxide as Visible-Light-Sensitive Photocatalyst: Designs, Developments, and Prospects. *Chemical Reviews*, 2014, vol. 114, pp. 9824-9852.

[6] BRECKENRIDGE, R. G., HOSLER, W.R. Electrical Properties of Titanium Dioxide Semiconductors. *Physical Review*, 1953, vol. 91, pp. 793-802.

[7] WANG, H., WANG, G., LING, Y., LEPERT, M., WANG, C., ZHANG, J. Z., LI, Y. Photoelectrochemical study of oxygen deficient TiO_2 nanowire arrays with CdS quantum dot sensitization. *Nanoscale*, 2012, vol. 4, pp. 1463.

[8] CHAE, S. Y., SUDHAGAR, P., FUJISHIMA, A., HWANG, Y.J., JOO, O.-S. Improved photoelectrochemical water oxidation kinetics using a TiO_2 nanorod array photoanode decorated with graphene oxide in a neutral pH solution. *Physical Chemistry Chemical Physics*, 2015, vol. 17, pp. 7714-7719.

[9] NOWOTNY, M. K., BAK, T., NOWOTNY, J. Electrical Properties and Defect Chemistry of TiO_2 Single Crystal. I. Electrical Conductivity. *The Journal of Physical Chemistry B*, 2006, vol. 110, pp. 16270-16282.

[10] TATARENKO, N. I., MOZALEV, A. M. Geometry and element composition of a nanoscale field emission array formed by self-organization in porous anodic aluminum oxide. *Solid-State Electronics*, 2001, vol. 45, pp. 1009-1016.

[11] CHANG, Y.-H., LIN, H.-W., CHEN, C. Growth Mechanism of Self-Assembled TiO_2 Nanorod Arrays on Si Substrates Fabricated by Ti Anodization. *Journal of the Electrochemical Society*, 2012, vol. 159, pp. D512-D517.

[12] BENDOVA, M., KOLÁŘ, J., HUBÁLEK, J., MOZALEV, A. Formation of TiO_2- based columnlike nanostructured anodic films on pure and doped titanium layers. In: *NANOCON 2015: 7th International Conference on Nanomaterials - Research and Application*, Ostrava: TANGER, 2015, pp. 64-64.

[13] BERANEK, R.: (Photo)electrochemical Methods for the Determination of the Band Edge Positions of TiO_2 -Based Nanomaterials. *Advances in Physical Chemistry*, 2011, pp. 1-20.

[14] PAN, X., YANG, M.-Q., FU, X., ZHANG, N., XU, Y.-J. Defective TiO_2 with oxygen vacancies: synthesis, properties and photocatalytic applications. *Nanoscale*, 2013, vol. 5, pp. 3601-3614.

[15] SEABOLD, J. A., CHOI, K.-S. Effect of a Cobalt-Based Oxygen Evolution Catalyst on the Stability and the Selectivity of Photo-Oxidation Reactions of a WO_3 Photoanode. *Chemistry Materials*, 2011, vol. 23, pp. 1105-1112.